



OPEN Numerical and experimental study of the optimal specimen geometry for direct tension strength tests in high tensile strength fiber reinforced concrete

Miguel A. Vicente¹✉, Álvaro Mena-Alonso¹, Dorys C. González¹, Gonzalo Ruiz², Héctor Cifuentes³, Carlos Leiva⁴, Rena Yu² & Jesús Mínguez¹

The accurate determination of the tensile strength of concrete is a topic of growing interest, especially driven by the new ultra-high tensile strength fiber-reinforced concretes. However, this is a complex task, as traditional methods provide inconsistent results (both splitting tensile test and 3-point bending test). The most robust method is the direct tensile test. However, in concrete, it poses a technical challenge that has not yet been satisfactorily solved. The aim of this study is the design of a test specimen that maximizes the percentage of successful failure and also allows a viable anchorage solution to the load application equipment, especially for high and ultra-high tensile strength concretes. An optimized geometry of a bone-shaped specimen that maximizes the probability of collapse occurring at the central neck is presented. First, a mathematical function of the generatrix of the bone-shape specimen is presented. The behavior of the solution is also analyzed numerically and statistically, comparing it with other commonly used solutions for direct tensile tests. Additionally, the design, fabrication, and calibration of a tailored cardan joint for load centering, thus minimizing its eccentricity and the dispersion of the results. Finally, the results of a static test campaign carried out on six carbon-fiber reinforced high tensile strength concrete specimens. The proposed bone-shaped specimen shows a much higher percentage of successful failures than the other specimen geometries commonly used for tensile testing, which improves the quality of tensile characterization test campaigns for high and ultra-high tensile strength concretes.

Keywords Ultra-high strength concrete, Direct tensile strength test, Fiber-reinforced concrete, Monte Carlo method, Cardan joint

Technological advances in the field of high performance concretes have led, in recent years, to the development of ultra-high tensile strength concretes^{1,2}. These concretes show, as a fundamental property, a much higher tensile strength than conventional ones, which is achieved either by modifying the microstructure of the cementitious matrix (incorporating, for example, nanoparticles)^{3–5}, or by including fibers^{6–9}. This also results in a substantial improvement of its ductility and fracture energy.

These materials provide interesting advantages in those concrete constructions where tensile stresses are moderate or low and can thus avoid the use of conventional reinforcement. These include pavements, weakly stressed footings, tunnels or dams, among many others^{10–12}.

In this context, the evaluation of the tensile strength of the material is essential, at the same level as its compressive strength. However, the accurate estimation of the tensile strength of concrete remains a technical challenge that has not been satisfactorily solved. Currently, the tensile strength of concrete is measured by indirect procedures, such as three-point bending tests (ASTM C1609/C1609M¹³, EN 14651:2005 + A1:2007¹⁴) or

¹Dpt. Civil Engineering, University of Burgos, C/ Villadiego s/n, 09001 Burgos, Spain. ²Dpt. Applied Mechanics and Project Engineering, University of Castilla – La Mancha, Ave. Camilo José Cela, 13005 Ciudad Real, Spain. ³Dpt. Continuum Mechanics and Structural Analysis, University of Seville, Camino de los Descubrimientos s/n, 41092 Seville, Spain. ⁴Dpt. Chemical and Environmental Engineering, University of Seville, Camino de los Descubrimientos s/n, 41092 Seville, Spain. ✉email: mvicente@ubu.es

the splitting tensile test (ASTM C496/C496M^{15,16}, EN 12390-6:2009¹⁶). The main advantage of these procedures is their ease of execution, using conventional laboratory equipment. However, their main limitation is that the tensile strength is obtained indirectly. Since the distribution of tensile stresses is not homogeneous throughout the specimen cross-section, the strength obtained by the two methods mentioned above is lower. Therefore, certain assumptions must be made to infer the indirect tensile strength from the direct tensile strength. Consequently, these traditional procedures are suitable for comparing concretes, but not for accurately determining their real tensile strength.

The only procedure that allows a real estimation of the tensile strength of concrete is the direct tensile test (DTT). This test is conceptually very simple: the specimen is subjected to an increasing tensile force until failure. The tensile strength is the quotient of the tensile force and the cross-section at failure. However, its realization involves solving a series of technical difficulties that, ultimately, are concentrated on the geometrical definition of the test specimen.

To date, the only standard regulating direct tensile strength tests in concrete is RILEM TC 162-TDF¹⁷, which employs a cylindrical specimen measuring 150 × 150 mm with a central annular notch 15 mm deep. The drawback of this approach is that failure originates at the edge of the annular notch, where a strong stress concentration occurs, and the stress field is far from uniaxial. Consequently, it cannot be assumed that the strength obtained corresponds to the uniaxial tensile strength of the concrete.

To address the issues related to stress concentration, direct tensile test standards typically use bone-shaped specimens with smooth transitions designed to ensure failure occurs in the central neck, where the stress state is more closely approximated to uniaxial tension. Examples include ASTM C190 for mortars, ASTM B557M for aluminum and magnesium alloys, ASTM E8/E8M for metallic materials, and ASTM D638 for plastics^{18–21}.

In recent years, numerous research studies have focused on evaluating the tensile strength of concrete^{22–36}. However, there is no consensus on the optimal specimen geometry, and the wide variety of shapes employed complicates the comparison of results across studies. Each specimen design presents its own set of advantages and limitations. Broadly, the specimens can be categorized into four geometric configurations, which are described below.

The first geometry is the cylindrical specimen^{24,31}. It is identical to the one used for compression tests. Its main drawback is the way of connecting the specimen to the testing machine to properly transmit the load. The most common solution is to glue the upper and lower flat faces of the specimen to the tensile machine using epoxy resins. The adhesive capacity of the resins is not very high, so the solution may be valid for conventional concretes, but not for high tensile strength concretes (where the tensile strength of concrete exceeds that of epoxy resin). Alternatively, a metal piece (i.e. a rebar) can be left embedded, as an anchor, at both ends and pulled³⁵. In both cases, significant stress concentrations occur in the bond regions of the specimen, leading in many cases to unsatisfactory failures. A variant of this geometry is the prismatic specimen, which shows the same advantages and disadvantages as the cylindrical one^{26,28}.

The second geometry is the cylindrical or prismatic specimen with a notch^{17,30}. This generates a plane of weakness in the specimen (usually centered on its length), so that failure always occurs in this plane. The disadvantage is that, in that region, there is a strong stress concentration; the stress field is far from being unidirectional and the estimation of the tensile strength is neither simple nor direct.

The third geometry is the “briquet” specimen, which is the one proposed in ASTM C190¹⁸. It is a biscuit-shaped specimen of small thickness. It has two rounded ends intended for gripping (requiring no adhesive) and a central neck, of smaller cross-section, where failure is expected to occur⁶. This solution presents two major problems. The first is that the cross-section of the specimen is variable along its entire length, so the stress state of the specimen is strongly two-dimensional, and quite complex. Again, estimation of the tensile strength of the material is neither simple nor straightforward. The second problem is that the specimen is cast according to a pour direction perpendicular to the tensile direction. This also occurs in the prismatic specimens of the geometries described above. In the case of plain concrete, this may not be a problem, but in the case of fiber-reinforced concrete, this fact can have a significant influence on the fiber orientation and, consequently, on the tensile strength.

The fourth geometry is the bone-shaped specimen. This solution is adopted because of its similarity to the specimens used in other materials (especially metallic materials). There are two versions of it. The first is the “cookie” type solution, with a rectangular cross-sections^{22,25,32–34,37,38}, and the second one is the revolving solution, with a circular cross-sections^{36–41}. In these specimens, three clearly differentiated parts are identified, namely, the central neck, whose section is constant and of minimum size, the extreme heads, whose section is constant and of larger size, and the transition regions that connect the central neck with the extreme heads. In all cases, the fixing of the specimen to the testing machine is made either by resin bonding or by means of an embedded steel bar.

The bone-shaped specimen is the most widely used specimen because it best balances the advantages and disadvantages. This geometry ensures that the maximum stresses do not occur at the ends, where the specimen is clamped to the testing machine. The test result is considered valid as long as the failure occurs within the central neck, where the stresses are appreciably uniaxial. Provided that the dimensions of the transition regions and extreme heads are adequate, the complex stress fields occurring in these regions will be small enough to prevent failure.

Among the bone-shaped specimens, the most common are the “cookie” type, due to their ease of fabrication (they require a simpler mold), although they present the problem that the casting direction does not coincide with the test direction. On the other hand, the revolving solution requires a more complex and, therefore, more expensive mold. Its main advantage is that the casting direction coincides with that used in the manufacture of cylinders for compression tests, so it is expected that the morphology of the microstructure and the orientation of the fibers will follow similar patterns in the specimens used for compression and tensile tests.

The bone-shaped specimen will behave correctly during the test if the failure occurs within the central neck, where the stress flow is essentially uniaxial tensile. In this case, the tensile strength of concrete is calculated as the quotient between the maximum tensile load and the cross-section of the neck. In addition, and similar to what is done with cylindrical specimens subjected to compression, it is possible to obtain the tensile stress-strain curve, the tensile modulus of elasticity or the Poisson's ratio, among other parameters.

However, for the bone-shaped specimen to behave correctly, it is necessary to carefully design its generatrix. In the most general case of a bone-shaped specimen, the generatrix is composed of three straight sections joined by two curved sections (Fig. 1).

The different specimens used in the research work carried out differ from each other precisely in the aforementioned transition sections. Thus, for example, the different solutions that can be found in the literature are classified into three large groups (Fig. 2).

A first group corresponds to those specimens in which the transition curve is simply a straight section forming a certain angle with the directrix. The generatrix is, in this case, a polygonal function composed of five straight sections. Some variants of this solution are a generatrix composed by four straight sections (without central neck), by three straight sections (without extreme heads), and even by two straight sections (without extreme heads and without central neck)^{38–40}.

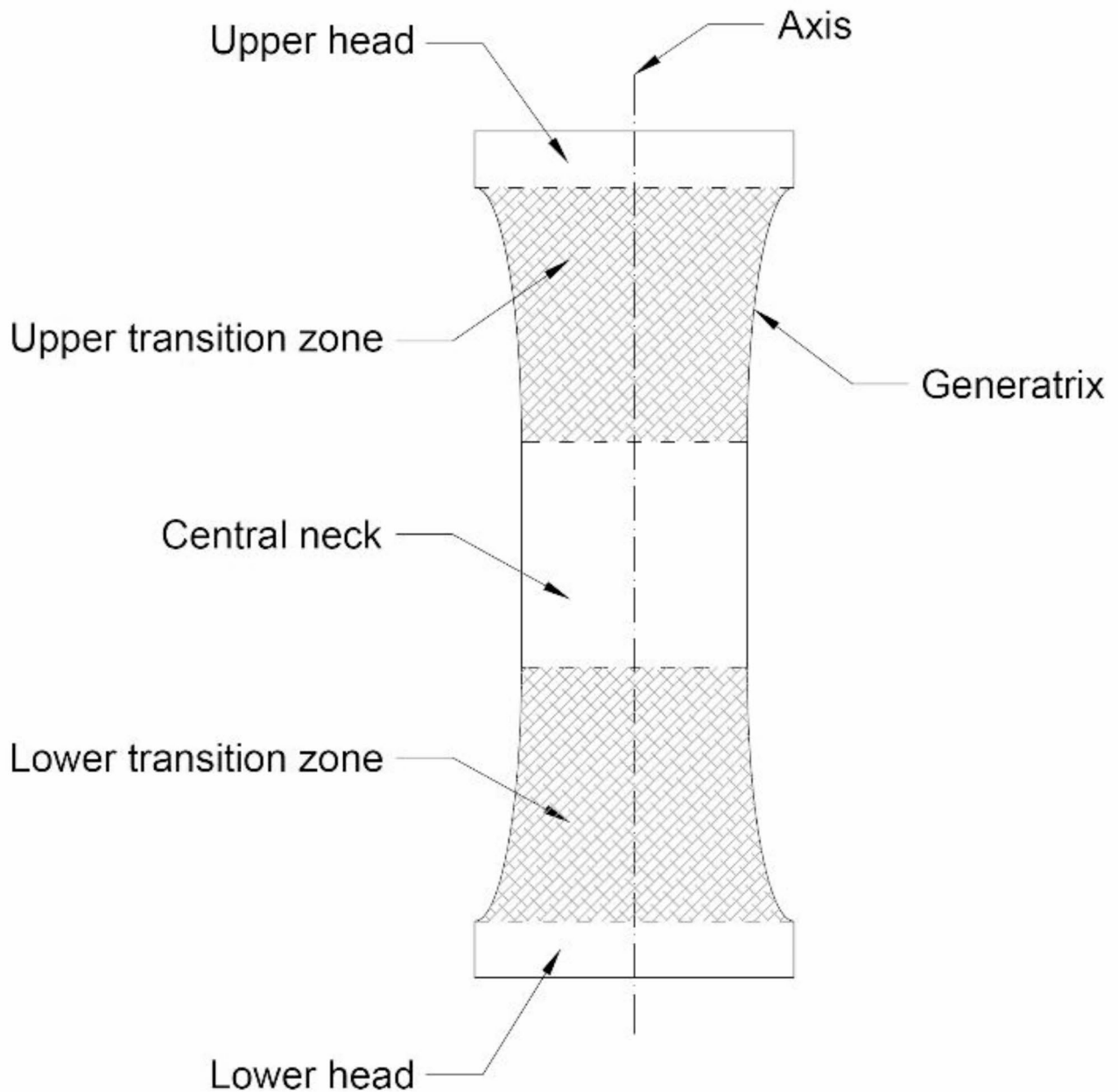


Fig. 1. Parts of a bone-shaped specimen.

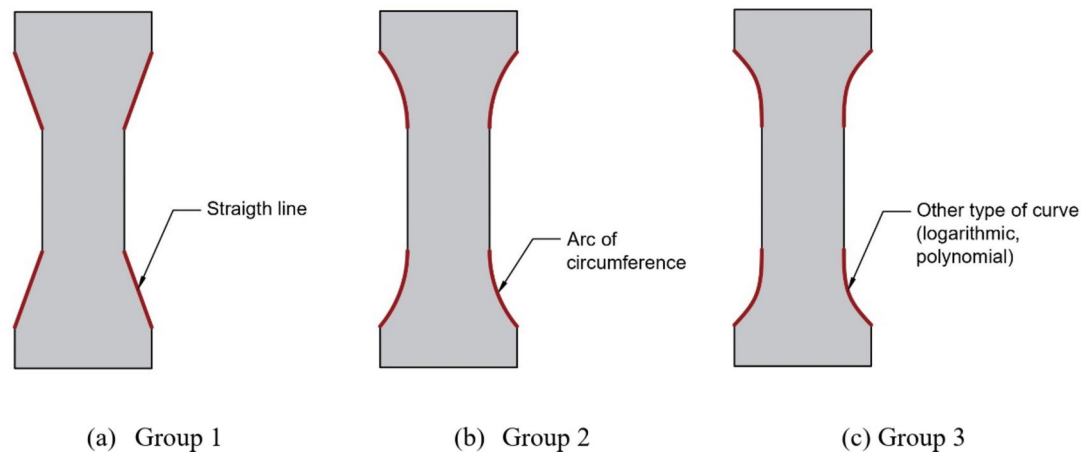


Fig. 2. Types of bone-shaped specimens depending on their geometry.

A second group corresponds to those specimens in which the transition curve is a circumferential arc. In all cases, the arc of the transition curve is tangent to the straight section that constitutes the central neck. In some cases, the arc of the transition curve is perpendicular to the straight section constituting the extreme head, while, in other cases, it is oblique³⁶.

There is a third group in which the transition curve shows a different geometry, which is neither a straight section nor an arc of circumference. Within this group is the proposal developed and patented by Vicente and collaborators⁴¹.

In this work, a specimen solution is proposed for direct tensile testing of high-strength fiber-reinforced concrete. The specimen features a revolution bone geometry, based on the patent by Vicente et al.⁴¹. The interest in this proposal lies in the fact that the geometry has been specifically designed to reduce stress concentration and maximize the probability of failure occurring in the desired region of the specimen. Therefore, it is considered a potential basis for the standardization of this type of test. The proposed specimen has been experimentally studied through a campaign of static tests. However, to fully validate the solution, tests considering multiple variables—such as the type of concrete (plain, with steel fibers, with plastic fibers), its strength, or the type and properties of the applied adhesive—are required.

Geometrical definition of the bone-shaped specimen

The proposed specimen has a geometry of revolution in which the generatrix defining its contour is composed of (Fig. 3):

- A central straight section, which has a first diameter D_1 and a first length H_1 ,
- Two extreme straight sections having a second diameter D_2 and a second length H_2 , and,
- Two transitional curved sections having a third length H_3 . In this case, the transition curves are polynomials of degree 2 or higher.

The exact geometrical definition of the generatrix is determined from the radius $r(z)$ of the specimen as a function of its height. Its mathematical expression is given in the following equation defined by five sections (Eq. (1)) (Fig. 4):

$$r(z) = \begin{cases} \frac{D_2}{2} & 0 \leq z \leq H_2 \\ \frac{D_1}{2} + \frac{D_2 - D_1}{2 \cdot (H_3)^{n+2}} \cdot (H_2 + H_3 - z)^{n+2} & H_2 < z \leq H_2 + H_3 \\ \frac{D_1}{2} & H_2 + H_3 < z \leq H_2 + H_3 + H_1 \\ \frac{D_1}{2} + \frac{D_2 - D_1}{2 \cdot (H_3)^{n+2}} \cdot (z - H_2 - H_3 - H_1)^{n+2} & H_2 + H_3 + H_1 < z \leq H_2 + 2 \cdot H_3 + H_1 \\ \frac{D_2}{2} & H_2 + 2 \cdot H_3 + H_1 < z \leq H \end{cases} \quad (1)$$

where n is an integer greater than or equal to 0, which defines the degree of the polynomial defining the upper and lower transition curves, and z is the height variable, associated to the Z-axis. In fact, this is not a unique proposal, but rather a family of solutions.

The bone-shaped specimen described in this paper is the solid enclosed in the surface created by revolution of the above mentioned generatrix around the axis of revolution (Z-axis). The coordinates of the points in space belonging to the solid that forms the specimen, (r, θ, z) are those that satisfy the following mathematical conditions (Eq. (2)):

$$\begin{cases} 0 \leq z \leq H \\ 0 \leq r \leq r(z) \\ 0 \leq \theta \leq 2\pi \end{cases} \quad (2)$$

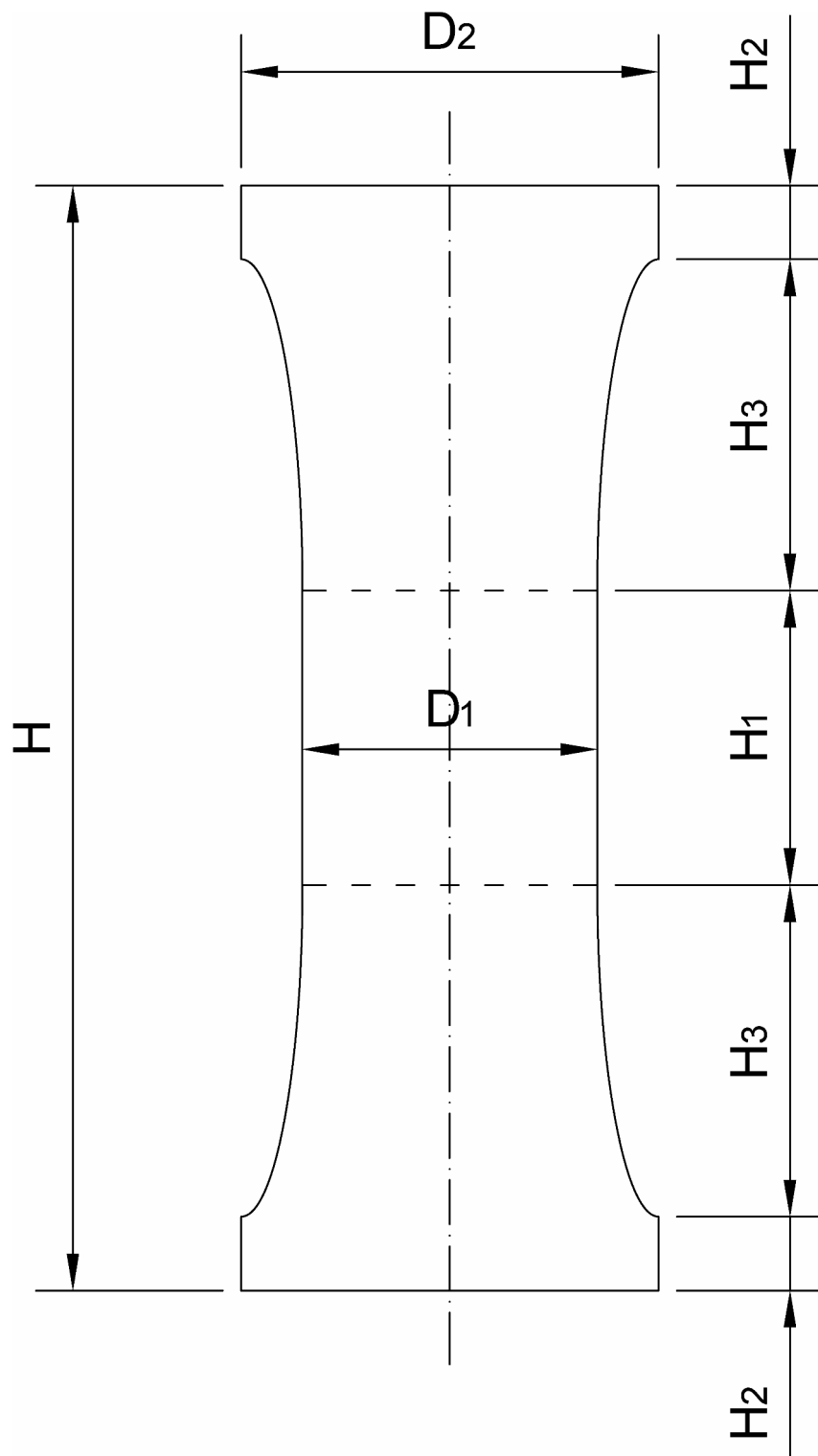


Fig. 3. Geometrical definition of the bone-shaped specimen.

Criteria for comparison of test specimens

The parameter for comparing the quality of the different solutions of bone-shaped specimens is the percentage of specimens that have an unsatisfactory failure, so that the lower the percentage of unsatisfactory failures, the better the solution. A failure is considered satisfactory when it occurs in a region where the stress state is predominantly uniaxial tension, allowing the tensile strength of the material to be calculated as the maximum applied load divided by the cross-sectional area. Conversely, unsatisfactory failures occur in areas where the

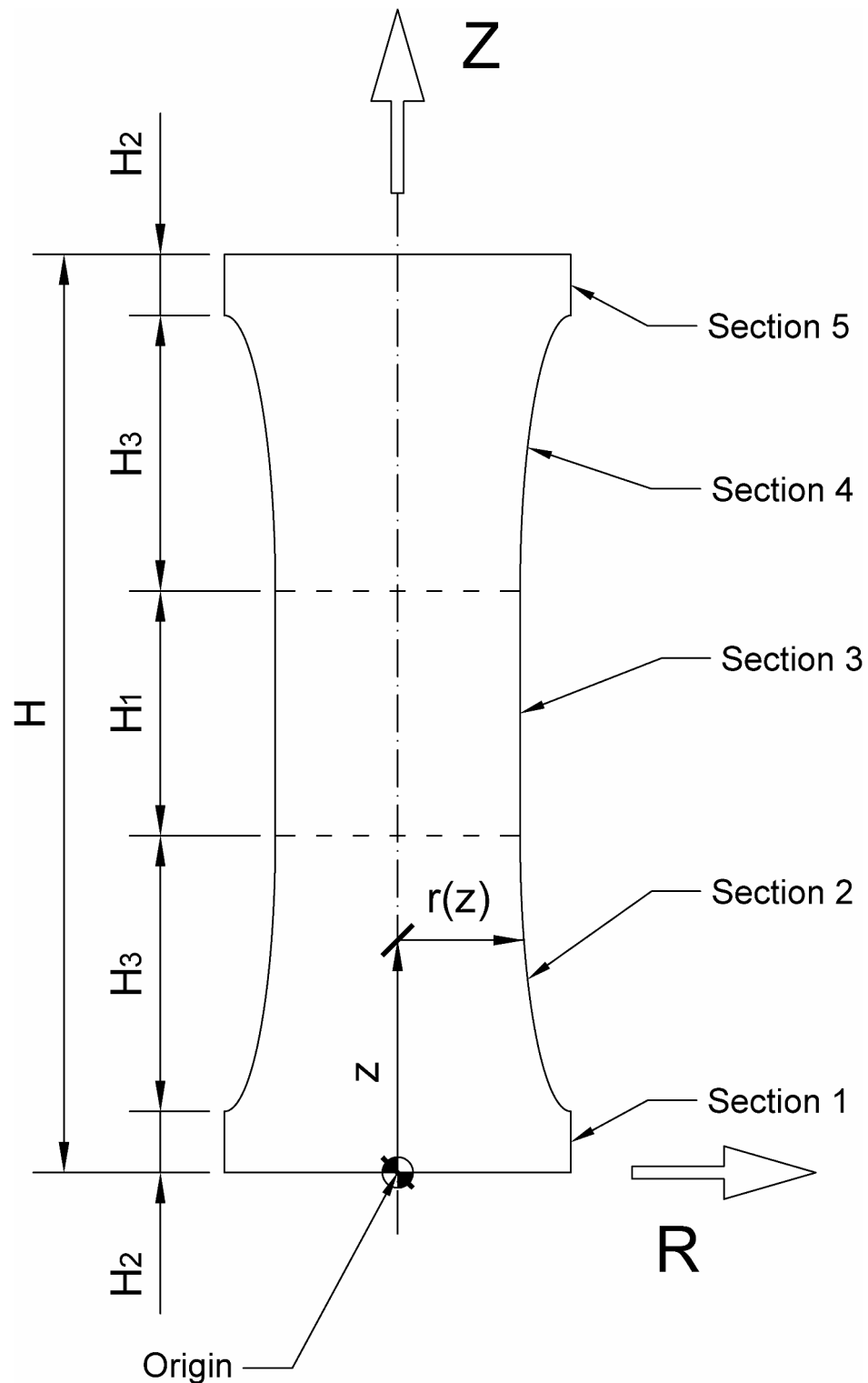


Fig. 4. Geometrical definition of the generatrix.

stress state is not uniaxial. In bone-shaped specimens, unsatisfactory failures typically occur in the transition zone between the ends and the central neck, where stress concentration phenomena are present.

Since concrete is a heterogeneous material, it is not possible to guarantee that the specimen will collapse at the desired region, although the probability is greater when the tensile stress in the central neck is closer to the maximum tensile stress in the specimen.

Therefore, from a theoretical point of view, it can be considered that the probability of unsatisfactory failure is lower, the higher the quotient between the maximum stress in the specimen and the maximum stress in

the central zone. The heterogeneity coefficient hc is, therefore, defined according to the following expression (Eq. (3)):

$$hc = \frac{\sigma_{3,max,gl}}{\sigma_{3,max,c_n}} \quad (3)$$

where $\sigma_{3,max,gl}$ is the maximum tensile principal stress in the specimen and σ_{3,max,c_n} is the maximum tensile principal stress in the central neck. The heterogeneity coefficient hc always shows values equal or greater than 1.

The smaller the coefficient of heterogeneity, the closer the maximum stress in the central neck is to the maximum stress in the specimen, so the more likely it is to provide satisfactory failure. Conversely, the higher the coefficient of heterogeneity, the more likely it is that the specimen will collapse at a section outside the central neck.

In order to compare different specimen geometries used by other researchers and to obtain the optimum one, finite element models are developed, considering a linear-elastic material. Using the data provided by the FE models, the principal tensile stress in the whole specimen and the principal tensile stress in the central neck are obtained, and, therefore, the heterogeneity coefficient hc of each geometry.

Numerical simulation of different solutions

The next step consists of calculating the heterogeneity coefficient of different specimen geometries, including some of those belonging to the family described in Sect. 2. For this purpose, finite element models of the different specimens have been developed. In all cases, a tensile load was applied so that the theoretical maximum principal stress, calculated as the load divided by the cross-sectional area of the central region, was 1 MPa. Thus, the value of the maximum principal tensile stress observed in the model is directly the coefficient of heterogeneity. Since the specimen presents symmetry of revolution, the stress map is perfectly characterized showing a half section according to a vertical plane passing through the axis of rotation.

Specifically, eleven solutions will be evaluated in this work. The first six ones correspond to the solution proposed in this work, for values of n between 0 and 5. In all cases, the total height of the specimen (H) is 150 mm, the height of sections 1 and 5 (H_2) is 10 mm respectively, the height of sections 2 and 4 (H_3) is 45 mm, the height of the neck (H_1) is 40 mm, the diameter of the central neck (D_1) is 40 mm and the diameter of the extreme heads (D_2) is 56.6 mm (Fig. 5).

In addition, five other types of specimens were evaluated, corresponding to geometries proposed by researchers as well as standards. Thus, solution no. 7 corresponds to the approach by Cornelissen & Timmers in 1981³⁶, no. 8 is the one by Jun & Mechtcherine in 2010³³, no. 9 represents the proposal by Wille et al. in 2011³², no. 10 pertains to the work of Kim et al. in 2021²², and no. 11 is the proposal from the RILEM TC 162-TDF standard of 2001¹⁷.

For each of the solutions, a finite element model has been developed considering a material with linear-elastic behavior, with a modulus of elasticity of 30 GPa and a Poisson's ratio of 0.2 (characteristic of concrete). The finite element models have been developed with the software ANSYS version 2023 R1 (ANSYS, Inc., Canonsburg, PA, USA).

Figure 6 shows the stress maps for each of the eleven solutions.

From the information gathered in Fig. 6, it is possible to determine the heterogeneity coefficients of each of the solutions, which are shown in Table 1.

The results show that the bone-shaped specimen solution described in this paper for the case of $n = 1$ has the lowest heterogeneity coefficient, which means that the probability of failure occurring in the central neck is higher.

In a concrete element (as in any other material), the failure does not necessarily occur at the point where the principal stress is the highest, but at the point where the applied stress is higher than its strength. The tensile strength of concrete is different at each point, due to the intrinsic heterogeneity of the material.

To numerically determine the probability of failure of each solution, a statistical calculation has been carried out, assigning to each element of the finite element model a random value of tensile strength, following a normal distribution, with $\mu = 1$ and $\sigma = 0.1$. The standard deviation value considered is usual in concretes, both in tension and compression^{23,27}.

Approximately, it can be considered that the specimen will collapse at the central neck whenever the minimum value of the tensile strength of the concrete located in the region of maximum stress will be hc times greater than the lowest value of the tensile strength of the concrete located at the neck.

To determine the probability values, a Monte Carlo model with 100,000 simulations has been developed. In each simulation, two values are obtained: the minimum stress value of the concrete located in the maximum stress region, from a set of points randomly chosen from this region, and the minimum stress value of the concrete located in the central neck, from a set of points randomly chosen from this region. The size of the set of points in each region is determined according to their relative size.

The simulation shows an out-of-neck failure (or, in other words, an unsatisfactory failure) if the minimum stress of the concrete located in the neck is less than hc times the minimum stress of the concrete located in the maximum stress region. Otherwise, the failure occurs at the neck.

Finally, the probability of obtaining a valid failure is defined as the quotient between the number of simulations in which the failure occurs at the neck and the number of simulations performed. The results are shown in Table 1.

The results in Table 1 reveal several interesting conclusions. First, it is observed that the performance of the proposed solution is highly sensitive to the polynomial degree of the transition curve. The best-performing

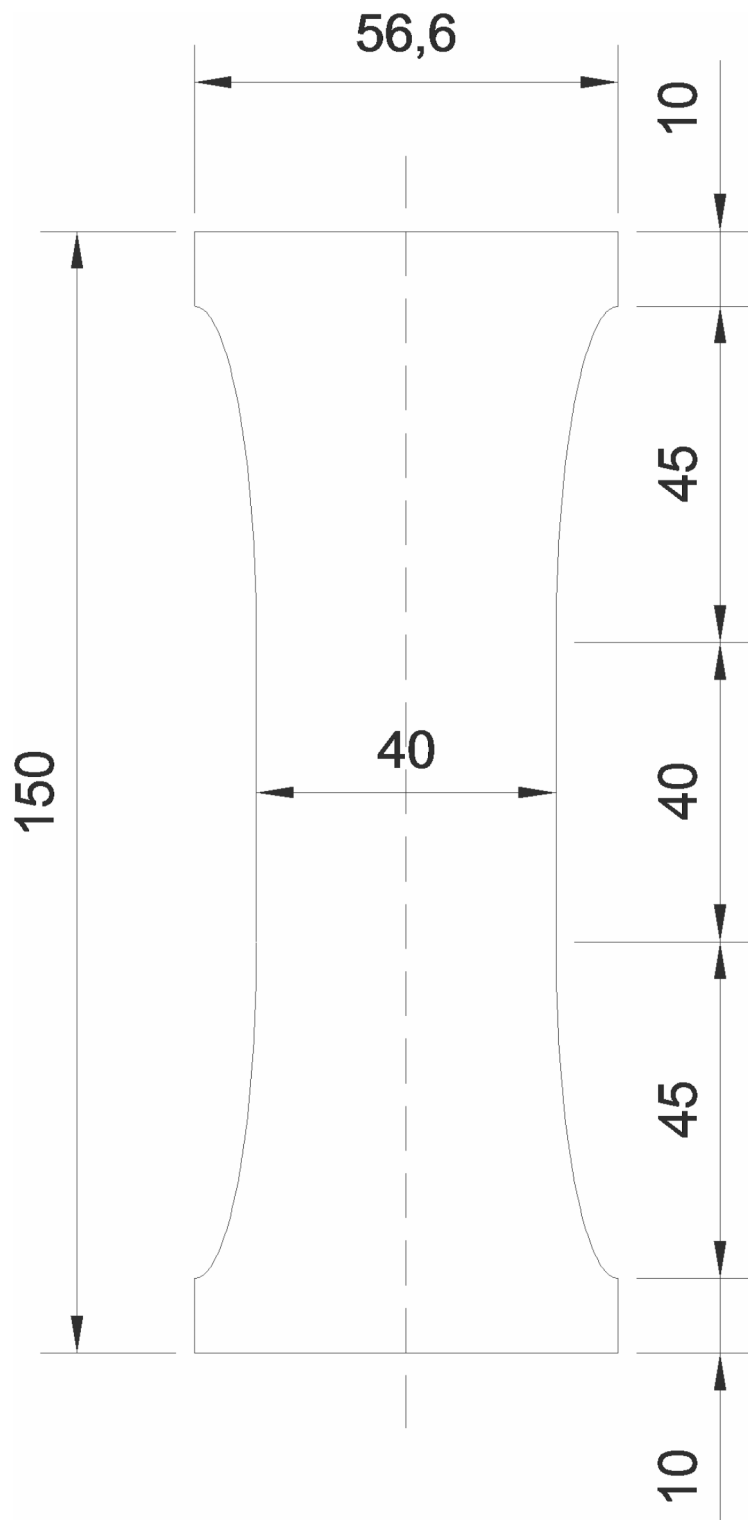


Fig. 5. Specific geometrical definition of the specimen.

bone-shaped specimen is achieved with $n = 1$, yielding a satisfactory failure probability of 84%. At the other extreme, for $n = 5$, the probability drops to only 16%. Regarding the specimens from the literature, the best results are obtained by the Jun & Mechtcherine³³ specimen, with a probability of 71%. For the rest of the specimens, failure in the central region under uniaxial stress is highly unlikely, with values below 1%. This is because their geometry and boundary conditions induce significant stress concentration phenomena that trigger failure outside the regions of interest.

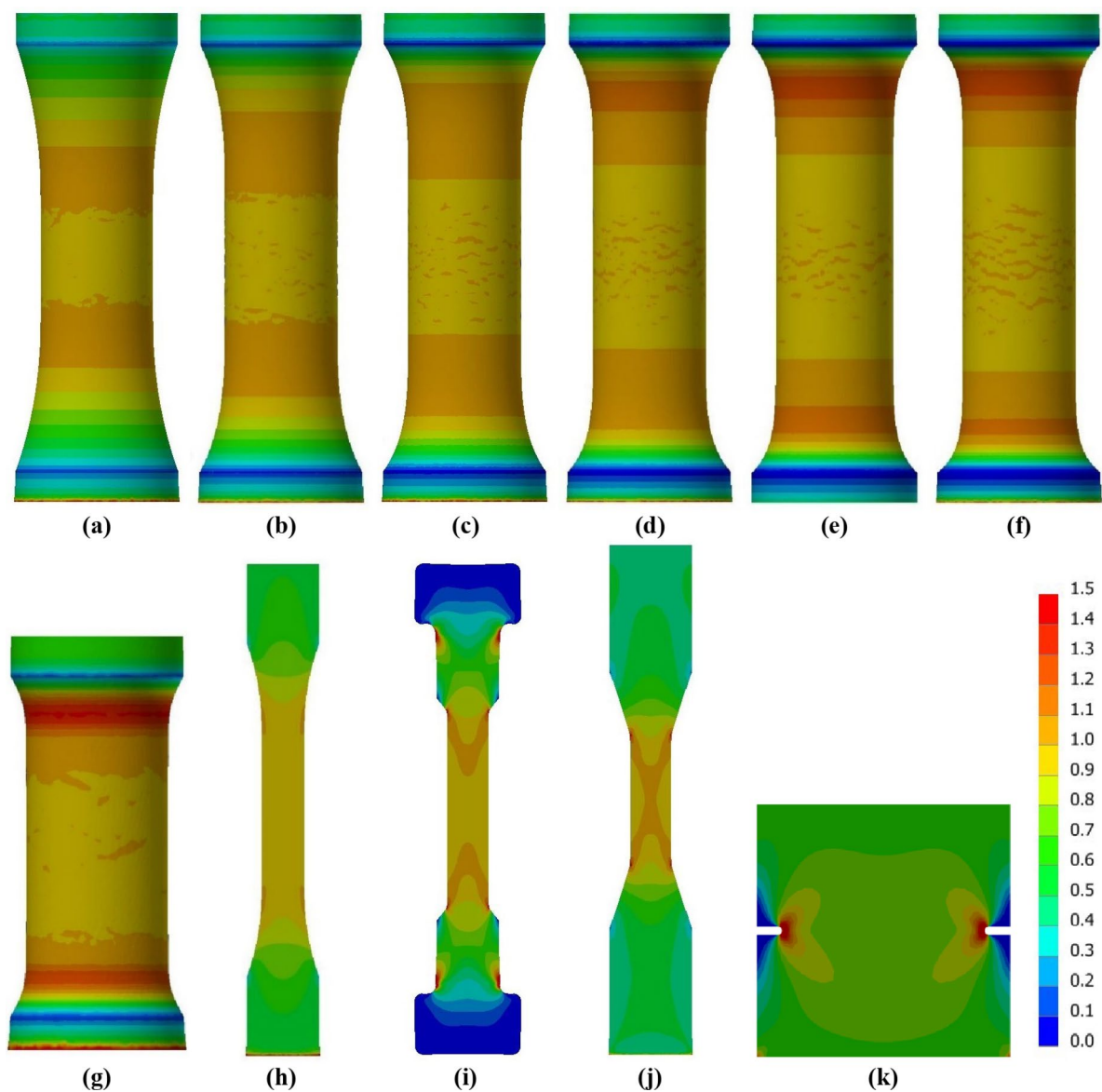


Fig. 6. Maximum principal stress map (in MPa) for a theoretical normal stress in the central neck of 1 MPa: (a–f) proposed with values of n from 0 to 5, (g) Cornelissen & Timmers³⁶, (h) Jun & Mechtcherine³³, (i) Wille, Kim and Naaman³², (j) Kim, Oh and Yoo²², (k) RILEM TC 162-TDF¹⁷ (finite element models have been developed with the software ANSYS version 2023 R1).

Specimen	hc	Probability of satisfactory failure
Proposed ($n=0$)	1.06	0.7984
Proposed ($n=1$)	1.04	0.8370
Proposed ($n=2$)	1.07	0.7653
Proposed ($n=3$)	1.13	0.5774
Proposed ($n=4$)	1.25	0.2008
Proposed ($n=5$)	1.27	0.1563
Cornelissen & Timmers [36]	1.43	0.0010
Jun & Mechtcherine [33]	1.09	0.7067
Wille, Kim & Naaman [32]	2.12	0.0003
Kim, Oh & Yoo [22]	1.94	0.0037
RILEM TC 162-TDF [17]	2.92	not applicable

Table 1. Stress heterogeneity coefficients hc and probability of satisfactory failure in the specimens studied.

With regard to the standardized specimen¹⁷, a clarification is necessary. Its geometry causes failure to always occur in the central neck, but not in a region under uniaxial tensile stress (which would correspond to the interior of the specimen). Instead, failure occurs at the edge of the notch, where there is significant stress concentration. Therefore, the probability of satisfactory failure here refers to failure in the central neck due to a uniaxial stress state. Consequently, the solution proposed by RILEM¹⁷ guarantees that failure occurs in the notch section and is a valid geometry to compare concretes under tensile loads. However, it is not valid to determine the tensile strength of concrete, since it cannot be defined as the ratio between the tensile load and the area of the notch section.

It is worth mentioning that, in some of the cited papers, the boundary conditions defining the connection between the specimen and the tooling applying the tension are not defined with sufficient precision. Therefore, with the available information, the properties of the specimen-to-tooling contacts (area, stiffness, etc.) have been estimated. Since these connections can significantly affect the stress concentration phenomena, it is possible that, in some cases, particularly those exhibiting a probability of success lower than 0.01, the behavior of the real solution may be better.

Experimental campaign

In order to be able to evaluate the behavior of the chosen solution, a tensile test campaign is carried out. In this case, the transition curve corresponding to $n = 1$ has been considered, which, as shown in Table 1, presents the lowest heterogeneity coefficient.

Materials and mix proportions

The binder materials utilized in this investigation were Type I Portland cement (52.5 R/SR), silica fume (SF) with a mean particle size of 0.1 μm , and ground granulated blast furnace slag (GGBS). Two aggregates were used: one with particles ranging from 800 to 80 μm and the other with particles ranging from 315 to 40 μm . To improve the workability of mixtures in their fresh form, a high-efficiency polycarboxylic ether-based superplasticizer (SP), namely Viscocrete 20HE manufactured by Sika (Baar, Switzerland), was used.

X-ray fluorescence spectrometer was performed to analyze the chemical compositions of the binder materials. The results are presented in Table 2.

The components and mix proportions employed are shown in Table 3.

All the specimens were manufactured using carbon fibers of 6 mm length and 7 μm diameter from Teijin (Osaka, Japan), with a proportion of 15 kg/m^3 . The tensile strength of the carbon fibers is 4,200 MPa. The Young's modulus is 230 GPa.

Specimen Preparation

One of the main drawbacks of the solution proposed in this research is the manufacture of the molds, since the geometry is complex.

The chosen specimen (150 mm height and 54 mm maximum diameter) fits in a conventional metal mold for cylindrical specimens (75 \times 150 mm). Using a 3D additive manufacturing printer, Ultimaker model S3 (Utrecht, Netherlands), a mold was made whose inner contour coincides with the geometry of the specimen and whose outer contour is a cylinder of 75 mm in diameter and 150 mm in height, fitting perfectly inside the aforementioned metal mold (Fig. 7).

The material used is PLA (polylactic acid) from Ultimaker, a recyclable natural thermoplastic polyester derived from renewable resources such as corn starch or sugar cane. It exhibits a tensile strength of approximately

	Cement	SF	GGBS
CaO	45.61	0.3	35.12
SiO ₂	18.29	79.58	27.81
Al ₂ O ₃	6.59	0.2	9.83
SO ₃	4.02	-	-
Fe ₂ O ₃	2.85	0.06	0.31
K ₂ O	1.09	0.42	2.01
MgO	1	0.35	6.63
TiO ₂	0.41	-	0.48
Na ₂ O	0.29	0.12	0.21
P ₂ O ₅	0.13	-	-
Cl ₂ O ₃	0.07	-	-
BaO	0.06	-	-
MnO ₂	0.05	-	0.11
SrO	0.05	-	0.08
CuO	0.04	-	-
ZnO	0.02	-	-
Total	80.57	81.03	82.59

Table 2. XRF chemical composition of the binder materials.

Components	UHPFRC (kg/m ³)
Cement (Type I cement 52.5 R/SR)	540
GGBS	310
Silica fume	210
Coarse quartz sand (< 800 μ m)	470
Fine quartz sand (< 315 μ m)	470
Superplasticizer	42
w/c ratio	0.38
w/binder ratio	0.19

Table 3. Matrix components and mix proportions.



(a)



(b)



(c)



(d)

Fig. 7. Manufacture of specimens: (a) preparation of the molds; (b) concrete pouring and curing, (c) removal of specimens, (d) final aspect of specimens.

50 MPa, an elasticity modulus of 3.2 GPa, and a rupture elongation of 4%, providing moderate stiffness and adequate toughness for low mechanical stress applications. Additionally, PLA allows parts to be produced with a high degree of precision, which is crucial in this case. For functional reasons (in particular, to facilitate stripping), the mold is divided into two halves.

The concrete mixes were produced utilizing a vertical mixer and a precise sequential technique. Initially, the coarsest (800- μm sand) and finest (SF or GGBS) were mixed, followed by the subsequent coarsest (315- μm sand) and the next finest (cement), and so on. The additions were mixed for 2 min each. The superplasticizer and water were introduced together. To achieve a suitable consistency, all components were thoroughly combined for 30 min. Once the concrete mixture had reached a high degree of homogeneity, fibers were added and mixed until a consistent fiber-concrete mass was achieved, enabling complete fiber integration. After 24 h, the samples were demolded, cured, and submerged in water for 28 days.

Cardan joint for load centering

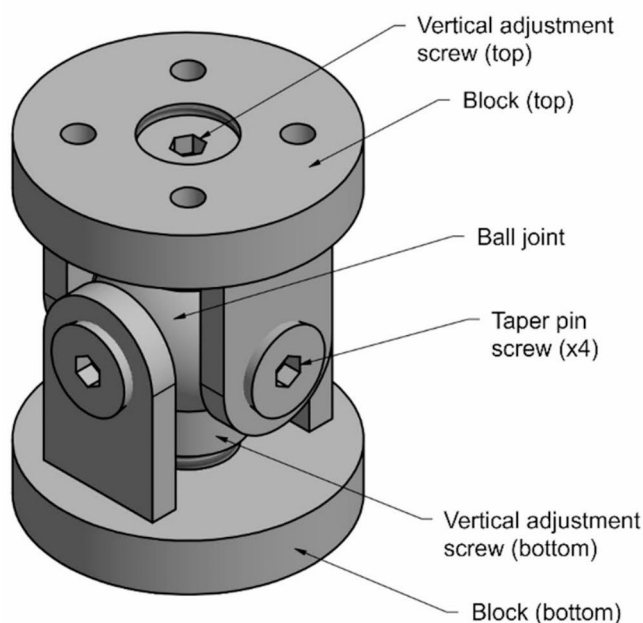
One of the most important aspects during the test is to ensure that the load is applied centered (i.e. with the minimum eccentricity with respect to the specimen axis). This is especially important in this specimen, because its diameter at the central neck is only 40 mm. Any eccentricity, however small, will generate a stress gradient that will greatly reduce the measured tensile strength.

Although the hydraulic actuator used to apply the load has two spherical plain bearings, these are too large and do not guarantee with sufficient precision that the load is applied at the desired point. For this reason, a cardan joint was designed specifically for these tests (Fig. 8).

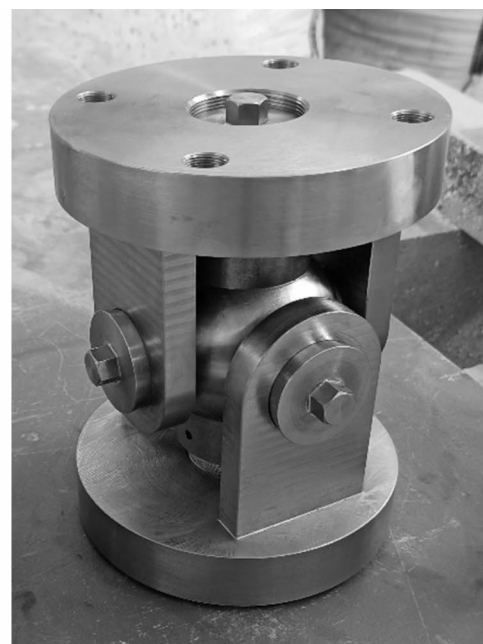
In this project, the cardan joint is used in a different way from the usual one. In this case, the aim of the cardan joint is to correct possible misalignments between the specimen axis and the load application axis (actuator axis). For this purpose, firstly, the cardan joint can rotate freely with respect to any axis perpendicular to the specimen axis (only rotation around the longitudinal axis of the cardan joint is prevented, but this is irrelevant in this case). Secondly, its geometry forces the applied load to circulate through the center of the sphere, correcting the eccentricity between the axis of the actuator and that of the specimen. In addition, the test bench ensures that both axes are parallel, which helps to further limit the eccentricity of the load.

The advantage of this type of cardan joint is that it allows centering the load in both tension and compression, which makes it suitable for all types of mechanical tests, including tensile, compression, or even cyclic with tensile-compression loads.

Figure 8.a shows the components of the cardan joint. The principle of operation under tension is as follows. First, the actuator applies the tensile load on the upper block. If the axes of the specimen and the actuator are not aligned, a relative rotation occurs between the upper and lower blocks. In that case, each block rotates a certain angle with respect to the axis defined by its taper pins. The taper pins are threaded into the central ball joint, while they are simply fitted into the lugs of the blocks. In this way, the blocks can rotate freely with respect to the taper pins. Once the rotation is corrected, the load is transmitted as follows. The taper pins transmit the shear load to the central sphere, so that the resultant necessarily passes through the center of the sphere. From there, the load is again transmitted by shear to the other taper pins, finally arriving centered at the lower block.



(a)



(b)

Fig. 8. Cardan joint for tensile tests. (a) Prototype design using CAD software, (b) Final unit manufactured in steel.

Tensile test Preparation

The preparation of the tensile test is more complex and laborious than in the case of compression or indirect tensile tests. First, the cardan joint is anchored to the test stand with a steel bolt system. The specimen is placed between the cardan joint and the actuator, connecting both sides with Sikadur-31 EF structural adhesive, manufactured by Sika (Baar, Switzerland). This is a two-component, thixotropic, epoxy resin-based adhesive. According to the data sheet provided by the manufacturer, its 24-hour tensile strength is approximately 10 MPa. The adhesive is applied as follows. First, a layer of about 10 mm is spread on both sides of the specimen. Then, the plunger of the actuator is lowered until it causes a small compression to the specimen (a small part of the resin overflows from the sides). The specimen is left in this position for 48 h to allow the resin to set, harden and have sufficient mechanical tensile strength to prevent the resin-specimen or resin-steel bond from breaking. This test set-up procedure also ensures that no hidden stresses are applied to the specimen that could condition the final failure mode (Fig. 9).

Results

Next, the most relevant results of the test campaign are shown.

Cardan joint validation tests

First, a validation test of the cardan joint was carried out to evaluate the eccentricity of the load during a tensile test. For this purpose, an aluminum bone-shaped specimen was used, with the same characteristics as described above. Three uniaxial strain gages of 50 mm length were arranged in the central section (SG1, SG2 and SG3), equispaced 120° in the position shown in Fig. 10.

From the strain data provided by the strain gages it is possible to determine the exact position of application of the tensile load by applying the equations of Mechanics of Materials (Eq. (4) to (6)).

$$e_x = \frac{3 \cdot \varphi}{16 \cdot (1 + \cos \theta)} \cdot \frac{\varepsilon_2 + \varepsilon_3 - 2 \cdot \varepsilon_1}{\varepsilon_1 + \varepsilon_2 + \varepsilon_3} \quad (4)$$

$$e_y = \frac{3 \cdot \varphi}{16 \cdot \sin \theta} \cdot \frac{\varepsilon_2 - \varepsilon_3}{\varepsilon_1 + \varepsilon_2 + \varepsilon_3} \quad (5)$$

$$e = \sqrt{e_x^2 + e_y^2} \quad (6)$$

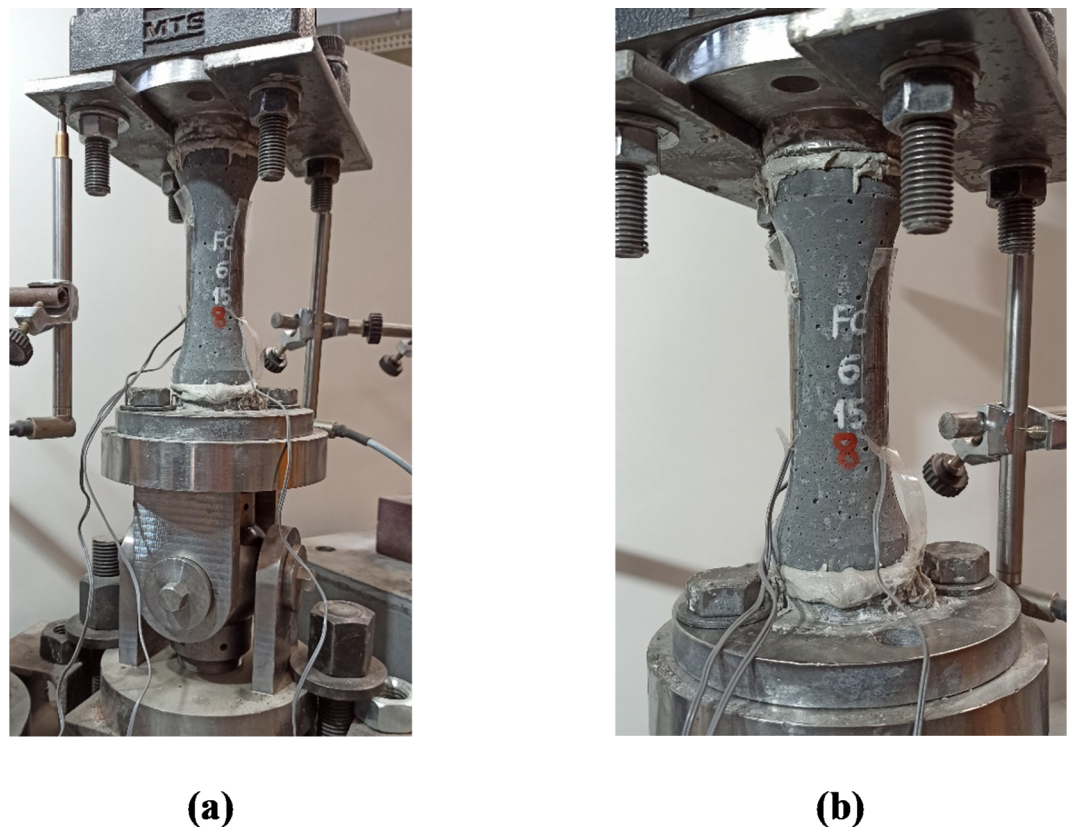


Fig. 9. Direct tensile test setup with bone specimen and cardan joint. (a) General view, (b) detail of the specimen and its connection with adhesive.

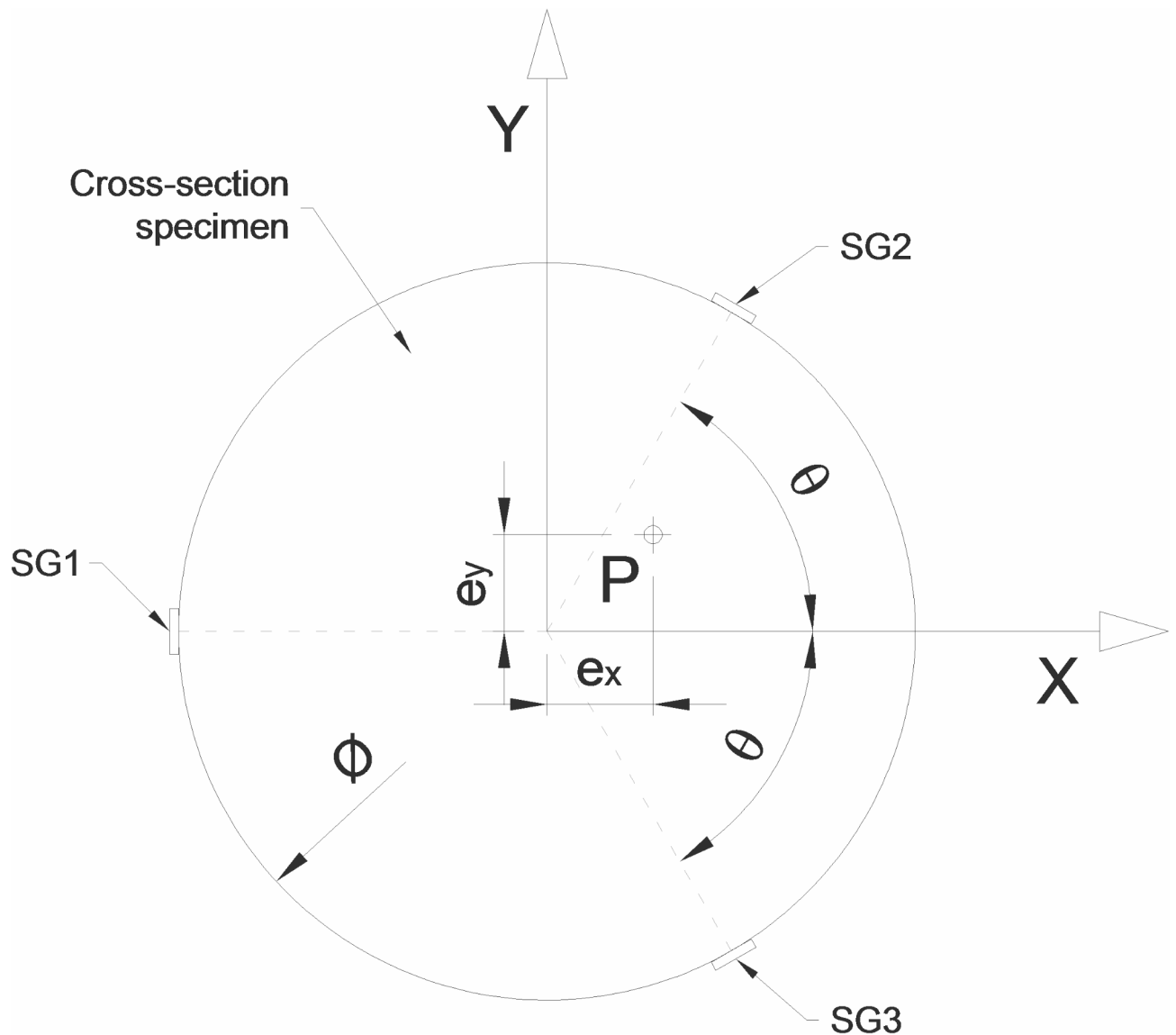


Fig. 10. Section of the specimen and scheme for the determination of the load eccentricity.

where ϵ_1 , ϵ_2 and ϵ_3 are the deformations measured by SG1, SG2 and SG3 bands respectively, ϕ is the diameter of the section (in this case, 40 mm) and θ is the angle that positions SG2 and SG3 bands with respect to the axes (in this case, $\pi/3$).

Figure 11 shows the eccentricity values measured in that test as a function of the applied load.

Figure 12 shows the position of the load throughout the test. In this figure, the outer circle represents the central section of the bone-shape specimen, while the inner circle represents the edge of the central core.

Figures 11 and 12 show how the load shows an eccentricity of less than 1.6 mm at all times. This is a low value (less than 32% of the center core edge), which certifies that the cardan joint performs its function successfully.

Tensile tests

Once the specimens had reached 56 days, tensile tests were performed. Unlike compression tests and indirect tensile tests, direct tensile tests require much more laborious preparation, as explained above. The test was carried out with displacement control. An MTS 244.21 dynamic actuator (MTS Systems, Eden Prairie, MN, USA) with a load range of ± 50 kN was used, fitted with an MTS 661.20 load cell with a range of ± 50 kN. The test speed was 0.5 mm/min.

Table 4 shows the tensile strength values of the specimens. Figure 13 shows the failure mode of all the specimens tested.

In this case, the tensile strength value of the material is not important for the purpose of this paper. However, it is interesting to note how the dispersion in tensile strength is quite low, which is a measure of the quality of the test. It is more interesting to note how all specimens failed at the center neck (Fig. 13).

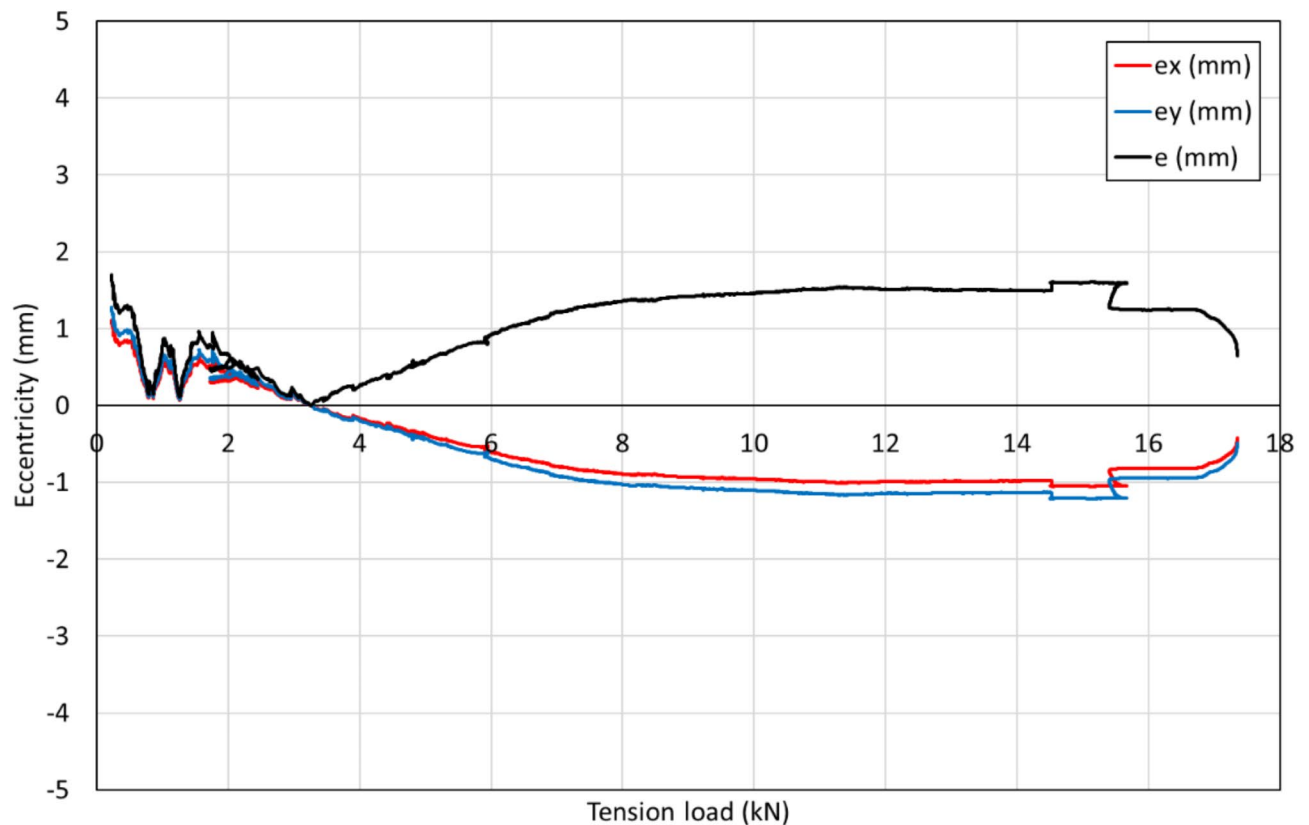


Fig. 11. Load eccentricity depending on the load.

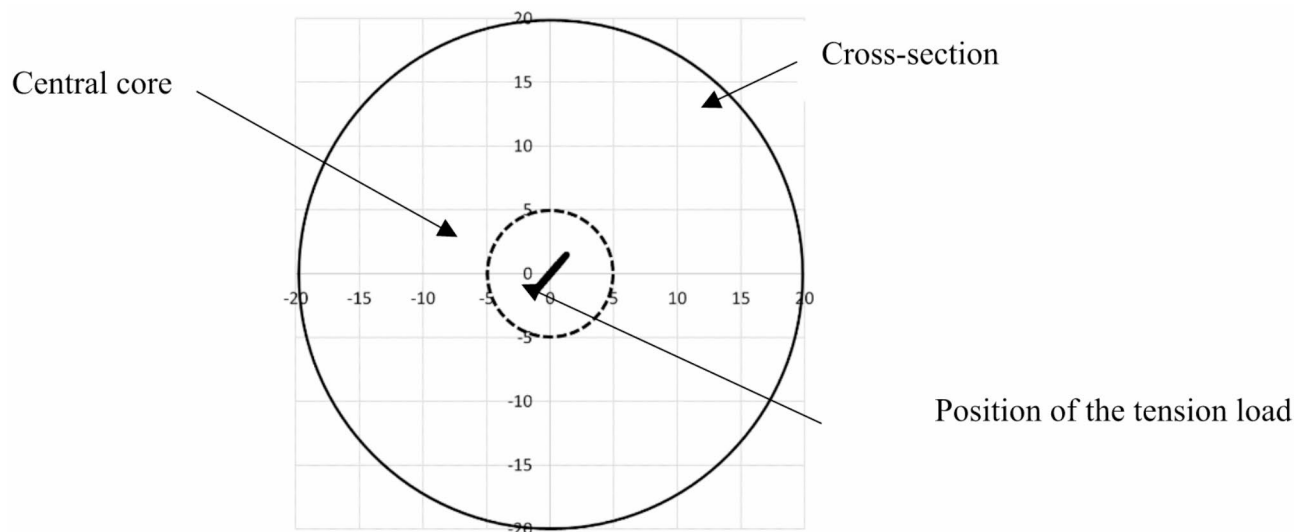


Fig. 12. Position of the load along the test.

In some cases, prior to specimen collapse, there was premature failure due to adhesion between the underside of the specimen and the adhesive. This was due to the fact that, since the lower face of the specimen is smooth, being the one in contact with the bottom of the mold, the bond with the adhesive is worse. In such cases, the adhesive was removed, the surface slightly eroded and the test preparation process was repeated.

In other cases, premature failure occurred according to a surface only a few millimeters below the contact between the top face of the specimen and the adhesive. This was because, during the casting process, a thin layer of less resistant material was created on top of the specimen. In addition, this layer was not sufficiently anchored

Specimen	P_{max} (kN)	f_c (MPa)	$f_{c,k}$ (MPa)
1	11.6	9.2	8.5 [0.5]
2	10.4	8.3	
3	9.9	7.8	
4	11.1	8.8	
5	10.2	8.1	
6	10.7	8.5	

Table 4. Tensile strength.



Fig. 13. Tensile failure of all the specimens.

to the rest of the matrix because it lacked fibers. In these cases, the adhesive was removed, the small layer was removed from the top of the specimen and the test preparation process was repeated.

Conclusions

This paper shows a new specimen solution with optimized geometry for direct tensile characterization of concrete. The aim is to define a geometry that maximizes the possibility of failure occurring in the central region, subjected only to uniaxial tension. In fact, a family of solutions is proposed, whose geometry conforms to a volume of revolution whose generatrix is composed of three straight sections and two curved sections according to a polynomial of degree $n + 2$.

In all cases, the maximum principal stress occurs outside the central neck of the specimen. However, among all the possibilities of this family, the case of $n = 1$ is the one that allows obtaining the heterogeneity coefficient hc closest to 1, expressed as the quotient between the maximum principal tensile stress and the tensile stress in the central zone of the specimen.

This study also analyzes the heterogeneity coefficients of other specimen geometries commonly used for the direct tensile characterization of concrete. In all the cases studied, their heterogeneity coefficients are clearly greater than 1 and, in some cases, really large values are obtained.

Even if the coefficient of heterogeneity is greater than 1, it does not necessarily mean that the specimen will not break in the central zone, which is explained by the intrinsic variability of the tensile strength in concrete. To evaluate the probability of failure in the central zone (successful failure), a Monte Carlo analysis was performed with 100,000 simulations per specimen, thus determining the probability of successful failure for each solution. The results show that the lower the heterogeneity coefficient, the higher the probability of successful failure.

To conclude, an experimental campaign was carried out on 6 specimens of 150 mm height and 40 mm diameter in the central area, which were subjected to a static tensile test until failure. The results showed that all specimens failed in the central zone, which demonstrates the quality of the proposed solution.

In order to improve load centering, a cardan joint was designed specifically for these specimens. The calibration results of the cardan joint showed eccentricity values lower than 1.6 mm, which confirms that it performs its function satisfactorily.

Data availability

Data is provided within the manuscript.

Received: 11 October 2024; Accepted: 13 March 2025

Published online: 28 March 2025

References

- Larsen, I. L. & Thorstensen, R. T. The influence of steel fibres on compressive and tensile strength of ultrahigh performance concrete: A review. *Constr. Build. Mater.* **256**, 119459 (2020).
- Yoo, D.-Y. & Banthia, N. Mechanical properties of ultra-high-performance fiber-reinforced concrete: A review. *Cem. Concr. Compos.* **73**, 267–280 (2016).
- Zhang, P., Wang, L., Wei, H. & Wang, J. A critical review on effect of nanomaterials on workability and mechanical properties of High-Performance concrete. *Adv. Civil Eng. Article ID. 8827124*, 24 (2021).
- Yazdchi, M., Foroughi Asl, A., Talatahari, S. & Gandomi, A. H. Evaluation of the mechanical properties of normal concrete containing Nano-MgO under Freeze–Thaw conditions by evolutionary intelligence. *Appl. Sci.* **11**, 2529 (2021).
- Khaloo, A., Mobini, M. H. & Hosseini, P. Influence of different types of nano-SiO₂ particles on properties of high-performance concrete. *Constr. Build. Mater.* **113**, 188–201 (2016).
- Oh, T., You, I., Banthia, N. & Yoo, D.-Y. Deposition of Nanosilica particles on fiber surface for improving interfacial bond and tensile performances of ultra-high-performance fiber-reinforced concrete. *Compos. Part. B.* **221**, 109030 (2021).
- Hu, A. X., Yu, J., Liang, X. W. & Shi, Q. Tensile characteristics of ultra-high-performance concrete. *Magazine Concrete Res.* **70**(6), 314–324 (2017).
- Park, S. H., Kim, D. J., Ryu, G. S. & Koh, K. T. Tensile behavior of ultra high performance hybrid fiber reinforced concrete. *Cement Concr. Compos.* **34**, 172–184 (2012).
- Song, P. S. & Hwang, S. Mechanical properties of high-strength steel fiber-reinforced concrete. *Constr. Build. Mater.* **18**(9), 669–673 (2004).
- Chan, R. et al. Analysis of potential use of fibre reinforced recycled aggregate concrete for sustainable pavements. *J. Clean. Prod.* **218**, 183–191 (2019).
- Salajegheh, P., Habibagahi, G. & Sahraeian, S. M. S. Utilizing fiber reinforced concrete as the concrete face of rockfill dams. *KSCCE J. Civ. Eng.* **23**(3), 1077–1086 (2019).
- Carmona, S., Molins, C., Aguado, A. & Mora, F. Distribution of fibers in SFRC segments for tunnel linings. *Tunn. Undergr. Space Technol.* **51**, 238–249 (2016).
- ASTM C1609/C1609M – 19a. *Standard Test Method for Flexural Performance of Fiber-Reinforced Concrete (Using Beam with Third-Point Loading)* (ASTM International, 2019).
- EN 14651:2005 + A1:2007. *Test Method for Metallic Fibre Concrete. Measuring the Flexural Tensile Strength (limit of Proportionality (LOP), residual)* (European Committee for Standardization (CEN), 2005).
- ASTM C496/C496M – 17. *Standard Test Method for Splitting Tensile Strength of Cylindrical Concrete Specimens* (ASTM International, 2017).
- EN 12390-6:2009. *Testing Hardened concrete - Tensile Splitting Strength of Test Specimens* (European Committee for Standardization (CEN), 2009).
- RILEM TC 162-TDF. *Test and design methods for steel fibre reinforced concrete - Uni-axial tension test for steel fibre reinforced concrete, Materials and Structures*, 34:3–6, France. (2001).
- ASTM C190–85. *Method of Test for Tensile Strength of Hydraulic Cement Mortars (Withdrawn 1990)* (ASTM International, 1990).
- ASTM B557M – 15. *Standard Test Methods for Tension Testing Wrought and Cast Aluminum- and Magnesium-Alloy Products (Metric)* (ASTM International, 2015).
- ASTM E8/E8M – 21. *Standard Test Methods for Tension Testing of Metallic Materials* (ASTM International, 2021).
- ASTM D638–14. *Standard Test Method for Tensile Properties of Plastics* (ASTM International, 2014).

22. Kim, M.-J., Oh, T. & Yoo, D.-Y. Influence of curing conditions on the mechanical performance of ultra-high-performance strain-hardening cementitious composites. *Archives Civil Mech. Eng.* **21**, 121 (2021).
23. Ferdosian, I. & Camoes, A. Mechanical performance and post-cracking behavior of self-compacting steel-fiber reinforced eco-efficient ultra-high performance concrete. *Cem. Concr. Compos.* **121**, 104050 (2021).
24. Chen, L. et al. Experimental and mesoscopic study of dynamic tensile properties of concrete using direct-tension technique. *Int. J. Impact Eng.* **155**, 103895 (2021).
25. Liao, W.-C., Chen, P.-S., Hung, C.-W. & Wagh, S. K. An innovative test method for tensile strength of concrete by applying the Strut-and-Tie methodology. *Materials* **13**, 2776 (2020).
26. Chen, X. & Chen, C. Experimental study on damage evolution behavior of Self-Compacting rubberized concrete under direct tensile fatigue loading. *KSCE J. Civ. Eng.* **24**(11), 3300–3308 (2020).
27. Goaiz, H. A., Farhan, N. A., Sheikh, M. N., Yu, T. & Hadi, M. N. S. Experimental evaluation of tensile strength test methods for steel fibre-reinforced concrete. *Magazine Concrete Res.* **71**(8), 385–394 (2019).
28. Goaiz, H. A., Yu, T. & Hadi, M. N. S. Quality evaluation tests for tensile strength of reactive powder concrete. *J. Mater. Civ. Eng.* **30**(5), 04018070 (2018).
29. Wille, K., El-Tawil, S. & Naaman, A. E. Properties of strain hardening ultra high performance fiber reinforced concrete (UHP-FRC) under direct tensile loading. *Cement Concr. Compos.* **48**, 53–66 (2014).
30. Lin, W.-T., Cheng, A., Huang, R. & Cheng, T.-C. A method for testing the strength of concrete using uniaxial direct tension. *J. Chin. Inst. Eng.* **36**(3), 395–303 (2013).
31. Wu, S., Chen, X. & Zhou, J. Tensile strength of concrete under static and intermediate strain rates: correlated results from different testing methods. *Nucl. Eng. Des.* **250**, 173–183 (2012).
32. Wille, K., Kim, D. J. & Naaman, A. E. Strain-hardening UHP-FRC with low fiber contents. *Mater. Struct.* **44**, 583–598 (2011).
33. Jun, P. & Mechtcherine, V. Behaviour of Strain-hardening Cement-based composites (SHCC) under monotonic and Cyclic tensile loading. Part I – Experimental investigations. *Cement Concr. Compos.* **23**, 801–809 (2010).
34. Olivito, R. S. & Zuccarello, F. A. An experimental study on the tensile strength of steel fiber reinforced concrete. *Compos. B.* **41**, 246–255 (2010).
35. Swaddiwudhipong, S., Lu, H.-R. & Wee, T.-H. Direct tension test and tensile strain capacity of concrete at early age. *Cem. Concr. Res.* **33**, 2077–2084 (2003).
36. Cornelisen, H. A. W. & Timmers, G. Fatigue of plain concrete in uniaxial tension and in alternating tension-compression. Report 5-81-7. Department of Civil Engineering, Delft University of Technology, Delft, Netherlands. (1981).
37. Benson, S. D. P. & Karihaloo, B. L. CARDIFRC – Development and mechanical properties. Part III: uniaxial tensile response and other mechanical properties. *Magazine Concrete Res.* **57**(8), 433–443 (2005).
38. Kamal, A., Kunieda, M., Naoshi, U. & Nakamura, H. Evaluation of crack opening performance of a repair material with strain hardening behavior. *Cement Concr. Compos.* **30**, 863–871 (2008).
39. Chanvillard, G. & Rigaud, S. Complete Characterization of tensile properties of DUCTAL UHP-FRC according to the French recommendations. In *Fourth International Workshop on High Performance Fiber Reinforced Cement, Composites (HPFRCC4)* 21–34 (2003).
40. Roth, M. J., Eamon, C. D., Slawson, T. R., Tonyan, T. D. & Dubey, A. Ultra-high-strength glass fiber-reinforced concrete: mechanical behavior and numerical modeling. *ACI Mater. J.* **107**(2), 185–194 (2010).
41. Vicente, M. A. et al. Spanish Patent No. ES2931848B2 Probeta de ensayos de tracción directa para hormigón y otros materiales conglomerantes secundarios. Grant date: June 6th, 2023 (2021).

Author contributions

All authors are co-inventors of the bone specimen shown in this paper. HB, CL, GR and RY have fabricated the molds and the concrete specimens. MAV, AMA, DCG and JM designed and fabricated the cardan joint and the aluminum specimen, and performed the laboratory tests. All authors reviewed the manuscript. The authors have accepted responsibility for the entire content of this manuscript and approved its submission.

Funding

The authors are grateful for the financial support from the Ministerio de Economía y Competitividad, PID2019-110928RB-C31, PID2019-110928RB-C32 and PID2019-110928RB-C33, Spain.

Declarations

Competing interests

The authors declare no competing interests.

Additional information

Correspondence and requests for materials should be addressed to M.A.V.

Reprints and permissions information is available at www.nature.com/reprints.

Publisher's note Springer Nature remains neutral with regard to jurisdictional claims in published maps and institutional affiliations.

Open Access This article is licensed under a Creative Commons Attribution-NonCommercial-NoDerivatives 4.0 International License, which permits any non-commercial use, sharing, distribution and reproduction in any medium or format, as long as you give appropriate credit to the original author(s) and the source, provide a link to the Creative Commons licence, and indicate if you modified the licensed material. You do not have permission under this licence to share adapted material derived from this article or parts of it. The images or other third party material in this article are included in the article's Creative Commons licence, unless indicated otherwise in a credit line to the material. If material is not included in the article's Creative Commons licence and your intended use is not permitted by statutory regulation or exceeds the permitted use, you will need to obtain permission directly from the copyright holder. To view a copy of this licence, visit <http://creativecommons.org/licenses/by-nc-nd/4.0/>.